

MRI Brain Tumor Image Enhancement Using LMMSE and Segmentation via Fast C-Means

Ngan V. T. Nguyen¹, Tuan V. Huynh², Liet V. Dang³
University of Science, Ho Chi Minh City, Vietnam^{1,2,3}
Vietnam National University, Ho Chi Minh City, Vietnam^{1,2,3}

Abstract—Brain MRI imaging revolutionizes tumor diagnosis, yet noise frequently obscures the images, complicating precise tumor identification and segmentation. This paper presents a comprehensive pipeline for brain MRI enhancement and tumor segmentation. The proposed method integrates Wavelet Packet Transform (WPT) and Linear Minimum Mean Square Error (LMMSE) filtering for effective noise reduction, combined with morphological operations for contrast enhancement. For segmentation, Fast C-Means clustering is employed, with the number of clusters automatically determined from histogram peaks. The tumor cluster is selected based on the highest centroid intensity and further refined by morphological operations to accurately delineate tumor borders. The approach is evaluated on the BraTS 2021 dataset, subject to Rician, Gaussian, and salt-and-pepper noise with intensities from 6% to 14%. Results demonstrate superior noise suppression compared to Denoising Convolutional Neural Networks (DnCNN) and Non-Local Means (NLM), maintaining structural integrity with a Structural Similarity Index (SSIM) of 0.43 for Rician noise at $\sigma = 6\%$. Segmentation performance remains stable, achieving Dice coefficients above 0.70, precision over 90%, and sensitivity between 75% to 81%, despite challenges posed by higher levels of salt-and-pepper noise. Tumor characteristics such as position and size correspond closely to ground truth, validating the effectiveness of the system in automating tumor delineation and providing reliable diagnostic assistance in neuro-oncology.

Keywords—Magnetic Resonance Imaging (MRI); brain tumor segmentation; image denoising; Wavelet Packet Transforms (WPT); Linear Minimum Mean Square Error (LMMSE); fast c-means clustering

I. INTRODUCTION

The brain governs essential physiological and cognitive functions, making its health critical to overall well-being. Brain tumors pose a serious threat, potentially leading to severe neurological impairments or death if not diagnosed and treated in time. Magnetic Resonance Imaging (MRI) is a widely used, noninvasive imaging technique that plays a central role in detecting and evaluating brain tumors. However, MRI images are often affected by noise, which can obscure important details and hinder accurate diagnosis.

Advanced noise reduction techniques are essential to improve MRI image clarity, enhancing the visibility of critical anatomical structures and assisting physicians in making precise clinical decisions. This work aims to improve brain MRI images by means of efficient noise reduction, image contrast enhancement, tumor segmentation, so enabling correct tumor segmentation.

Our approach integrates the wavelet packet transform (WPT) for noise reduction with linear minimum mean square

error (LMMSE) filtering and morphological operations. The WPT decomposes the MRI images into subbands, enabling noise attenuation through shrinkage thresholding. The processed output then serves as input for both LMMSE filtering [1], which is effective in handling Rician noise common in MRI, and morphological operators [2] that enhance image contrast and structural details. The fusion of these outputs yields a noise-reduced, contrast-enhanced image without altering the original pixel distribution, making it suitable for subsequent segmentation or classification tasks.

For tumor segmentation, we apply the Fast C-means clustering algorithm, well-known for computational efficiency and better performance than conventional clustering techniques [3], for tumor segmentation. This method divides image intensities into logical clusters to precisely locate tumor areas. Morphological operations improve these segmented regions even more to precisely define tumor limits [4].

Though segmentation techniques and noise reduction have made great progress, integrating approaches that handle several noise types while maintaining image features essential for clinical interpretation remains difficult. Furthermore important factors for pragmatic uses are still computational efficiency and accuracy. This paper addresses these issues by suggesting a combined system for noise reduction and tumor segmentation catered to brain MRI images. This system helps to create Computer-Aided Detection (CADe) technologies, which have advanced quickly in recent years and improve diagnosis accuracy and patient outcomes by means of their support.

II. RELATED WORK

Brain MRI denoising and tumor segmentation have attracted considerable research attention because of their critical roles in accurate diagnosis and treatment planning. Conventional noise reduction methods such as Gaussian, median, and anisotropic diffusion filters have been applied widely. However, these linear or nonlinear filters often lead to blurring or loss of important anatomical details, negatively impacting diagnostic accuracy. Advanced methods have thus been created to overcome these constraints.

Wavelet transform-based methods have shown significant advantages for MRI noise reduction due to their ability to decompose images into multi-scale subbands, allowing selective attenuation of noise while preserving edges and fine details. While traditional wavelet thresholding methods successfully lower noise, in complex MRI data they may cause incomplete noise suppression or ringing artefacts. The Wavelet Packet Transform (WPT), a generalized form of wavelet decomposition, provides more flexible frequency band partitioning,

leading to better adaptability for MRI denoising tasks. Kinani et al. [1] proposed a combined approach that integrates WPT with the Linear Minimum Mean Square Error (LMMSE) filter to specifically address the Rician noise model in MRI. Their method demonstrated superior noise suppression and detail preservation compared to classical denoising filters.

In addition to noise reduction, enhancing the contrast and structural visibility of brain MRI is crucial for subsequent tumor detection and segmentation. Morphological operations have been successfully employed in this context to refine image features and remove residual noise artifacts. Hytch et al. [2] illustrated the use of morphological filters to improve local contrast without altering the overall pixel intensity distribution, thus preserving diagnostically relevant information.

Tumor segmentation is another challenging problem due to the heterogeneous shape, size, and intensity of brain tumors. Clustering-based algorithms, including K-means and Fuzzy C-means, are commonly applied for their ability to partition image pixels into distinct classes based on intensity or texture features. Classical clustering techniques, however, can be sensitive to initial conditions and have high computational cost, so restricting their useful value. Nawaz et al. [3] introduced the Fast C-means clustering algorithm, which reduces computation time and enhances segmentation accuracy by efficiently grouping data points. Their results confirm that Fast C-means outperforms traditional clustering in medical image segmentation, making it well-suited for tumor delineation tasks.

Further refinement of segmentation boundaries using morphological processing is essential to eliminate noise, fill gaps, and define tumor edges more precisely. D. S. et al. [4] applied morphological operations after clustering to improve tumor segmentation outcomes, yielding clearer and more accurate tumor borders.

Despite these advancements, current approaches face challenges in effectively balancing noise reduction, contrast enhancement, and segmentation accuracy within a unified framework. Many current techniques either separately reduce noise or enhance contrast, which can produce less than ideal outcomes or change pixel intensity distribution. Furthermore, the computational complexity of multi-stage procedures could make their implementation difficult in clinical environments where near real-time or real-time results are sought for.

Our work addresses these limitations by proposing a novel fusion strategy that integrates WPT-based noise reduction, LMMSE filtering, and morphological contrast enhancement to generate a quality-enhanced MRI image. After that, morphological refinement and Fast C-means clustering help to segment this image. The fusion method guarantees efficient noise suppression and contrast enhancement without distortion of the pixel intensity distribution, so enabling more accurate and dependable tumor segmentation. This integrated system contributes to the ongoing development of Computer-Aided Detection (CADe) systems, which are increasingly critical for early diagnosis and treatment of brain tumors.

III. METHODOLOGY

A. Summary Background Theories

1) *Wavelet packet decomposition*: The wavelet transform is a mathematical method that decomposes spatial (or temporal) data into spatial (temporal)-frequency domain components, allowing dominant frequency modes to be identified and their variations over space. The wavelet transform has been extensively utilized in a variety of disciplines, such as engineering, computer science, science, etc. due to its efficacy [5]. The discrete wavelet transform (DWT) stands out as a particular example.

During the DWT decomposition process, a signal is successively divided into multiple components, each represented by a set of coefficients that delineate the temporal progression of the data within a certain frequency bandwidth. The DWT utilizes two filters: a high-pass filter, based on the wavelet function, to produce detail components (coefficients) containing high frequencies, and a low-pass filter, based on the scaling function, to produce approximation components (coefficients) containing low frequencies. The quantity of breakdown stages, referred to as levels, aligns with particular scales that are inversely proportional to frequency. Since each level uses two filters, the approximate and detailed coefficients must be dyadic down-sampled so that the total length of these coefficients is equal to the length of the input signal. From level two and above, the above process is repeated with input being the approximate coefficient at the previous level.

Wavelet packet decomposition (WPD) enhances the functionality of discrete wavelet transform (DWT) by implementing the filtering procedure on both approximation and detail components at every level. This methodology enables WPD to deliver a more comprehensive depiction of the signal within tighter frequency bands, especially at elevated frequencies, in contrast to conventional DWT [6].

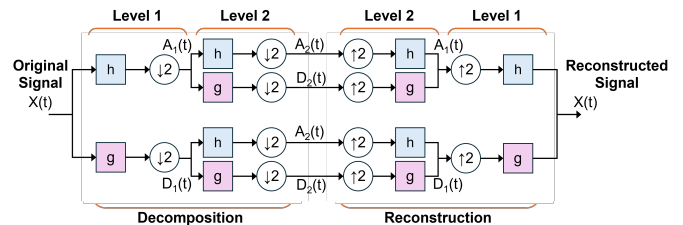


Fig. 1. The Processes for wavelet packet decomposition steps of 1D signal at 2 levels.

Wavelet packet reconstruction refers to the recovery of data that has undergone decomposition using wavelet packet decomposition (WPD). This entails upsampling the coefficients by interspersing zeros and utilizing them as inputs for reconstruction via low-pass and high-pass filters. The results are subsequently aggregated to reconstruct the original data structure. Fig. 1 depicts the wavelet packet decomposition and reconstruction procedure at level 2 [5].

2) *Linear minimum mean square error estimator*: The Linear Minimum Mean Square Error (LMMSE) estimator seeks to derive the closed-form representation of a signal that adheres to the Rician distribution [7]. Let q represent a scalar parameter derived from a dataset x in the following manner:

$$\hat{\theta} = \sum_{n=0}^{N-1} a_n x[n] + a_N \quad (1)$$

the weight coefficients are calculated by minimizing Bayesian MSE such that nonzero means of x and θ :

$$\text{Bmse}(\hat{\theta}) = E \left[(\theta - \hat{\theta})^2 \right] \quad (2)$$

where, the expectation is calculated according to the PDF $p(\mathbf{x}, \mathbf{q})$.

Substitute (1) into (2) and set the differential of (2) with respect to a_N to zero to determine a_N and substitute a_N into $\text{Bmse}(\hat{\theta})$; then, minimize this expression to obtain the LMMSE estimator [7]:

$$\hat{\theta} = E(\theta) + \mathbf{C}_{\theta x} \mathbf{C}_{xx}^{-1} (\mathbf{x} - E(\mathbf{x})) \quad (3)$$

where, \mathbf{C}_{xx} is the $N \times N$ covariance matrix of x , and $\mathbf{C}_{\theta x}$ is the $1 \times N$ cross-covariance vector. With a 2D signal with Rician distribution, (3) rewrite in the form [8]:

$$\hat{A}_{ij}^2 = E\{A_{ij}^2\} + \mathbf{C}_{A_{ij}^2 M_{ij}^2} \mathbf{C}_{M_{ij}^2 M_{ij}^2}^{-1} (M_{ij}^2 - E\{M_{ij}^2\}) \quad (4)$$

where, A_{ij} is an unknown pixel intensity value at (i, j) , M_{ij} is the brightness magnitude of the signal. By simplifying the estimation at each location, the vectors and matrices reduce to scalar values, and the estimator is expressed as:

$$\hat{A}_{ij}^2 = E\{A_{ij}^2\} + \frac{E\{A_{ij}^4\} + 2E\{A_{ij}^2\}\sigma_n^2 - E\{A_{ij}^2\}E\{M_{ij}^2\}}{E\{M_{ij}^4\} - (E\{M_{ij}^2\})^2} \times (M_{ij}^2 - E\{M_{ij}^2\}) \quad (5)$$

Under the assumption of local ergodicity, the expectation can be substituted with the sample estimate $\langle \cdot \rangle$; following some algebraic manipulations, the estimator is expressed as:

$$\hat{A}_{ij}^2 = \langle M_{ij}^2 \rangle - 2\sigma_n^2 + K_{ij}(M_{ij}^2 - \langle M_{ij}^2 \rangle) \quad (6)$$

where, K_{ij} is defined as:

$$K_{ij} = 1 - \frac{4\sigma_n^2(\langle M_{ij}^2 \rangle - \sigma_n^2)}{\langle M_{ij}^4 \rangle - \langle M_{ij}^2 \rangle^2} \quad (7)$$

with $\eta_{i,j}$ a square neighborhood around pixel [8].

B. Fast C-Means Clustering

Tumor segmentation is a critical phase in MRI image processing, with numerous approaches developed, the most prevalent being fuzzy clustering, recognized for its capacity to maintain the details of the original image [9]. Nonetheless, conventional fuzzy C-means is inefficient due to the necessity of computing the distance between each pixel and the cluster centers to minimize the objective function. Consequently, numerous enhanced techniques have been suggested that substitute pixel values with histogram gray levels to expedite computation. The enhanced C-means algorithm, founded on morphological reconstruction and membership filtering (FR-FCM), was proposed by Tao-Lei et al. [10].

The objective function is defined as:

$$S_\alpha = \sum_{n=1}^r \sum_{m=1}^d \lambda_n w_{mn}^\alpha \|\zeta_n - c_m\|^2, \quad (8)$$

Consider that w_{mn} indicates the degree of association for intensity level n concerning the m^{th} cluster centroid c_m , while α serves as the weighting coefficient. Then, we have:

$$\sum_{n=1}^r \lambda_n = M, \quad (9)$$

where, ζ represents an image reconstructed through morphological processing, and ζ_n corresponds to a specific intensity level, with $1 \leq n \leq r$. The parameter r signifies the count of intensity levels in ζ , which is typically much smaller than M . The reconstructed image ζ is obtained as:

$$\zeta = T^B(g), \quad (10)$$

where, T^B refers to the morphological reconstruction using a closing transformation, and g denotes the original image. Minimize (8) to obtain:

$$w_{mn} = \frac{\|\zeta_n - c_m\|^{-2/(\alpha-1)}}{\sum_{t=1}^d \|\zeta_n - c_t\|^{-2/(\alpha-1)}}, \quad (11)$$

and

$$c_m = \frac{\sum_{n=1}^d \gamma_n w_{mn}^\alpha \zeta_n}{\sum_{n=1}^d \gamma_n w_{mn}^\alpha}. \quad (12)$$

If we assign $W = [w_{mn}]^{d \times r}$ is membership partition matrix; w_{nt} and c_m are calculated using the iterative method until W stabilizes:

$$\max\{W(\tau) - W(\tau + 1)\} < \epsilon \quad (13)$$

where, ϵ is minimal error threshold. At that time, the new membership matrix $W' = [w_{mn}]^{d \times M}$ corresponding to the original image g :

$$w_{mn} = w_{mn}^{(\tau)}, \quad \text{if } y_n = \zeta_m \quad (14)$$

To enhance the membership partition matrix and accelerate convergence through membership filtering:

$$W'' = medW' \quad (15)$$

where, *med* represents median filtering

Fast C-Means is more appropriate for medical imaging applications due to its reduced computational cost and faster convergence compared to conventional FCM.

C. Morphological Contrast Enhancement

Morphological operations process the shape and structure of objects in images based on structural elements (SE), which can be considered as filters. There are four basic operations: dilation, erosion, opening (denoted as \circ), and closing (denoted as \bullet). Opening removes noise or small objects (relative to the SE size), while closing fills small holes and gaps in objects. The top-hat transform, defined as the difference between the image and the opening operation, is used to highlight bright objects (smaller than the SE) against a dark background. The bottom-hat transform, defined as the difference between the closing operation and the image, is used to highlight dark objects against a bright background. Combining these two transformations with the noise-reduced image produces an image with high contrast without pixel redistribution, thus preserving the accurate position of objects when detected [11].

The Tophat transform is defined as:

$$T(i, j) = P(i, j) - (P \circ S)(i, j) \quad (16)$$

The Bottomhat transform is given by:

$$B(i, j) = (P \bullet S)(i, j) - P(i, j) \quad (17)$$

where, $T(i, j)$ and $B(i, j)$ represent the top-hat and bottom-hat transforms, respectively; $P(i, j)$ denotes the noise-reduced image; S is the structuring element; $(P \circ S)$ refers to the morphological opening operation, and $(P \bullet S)$ represents the closing operation.

For image contrast enhancement, the final transformed image is computed as:

$$M(i, j) = (P(i, j) + T(i, j)) - B(i, j) \quad (18)$$

where, $M(i, j)$ is the enhanced image obtained by incorporating both top-hat and bottom-hat transformations to improve contrast.

D. Performance Evaluation

The enhancement algorithm aims to augment image quality, guaranteeing that the processed image is more appropriate than the original for further applications or analysis. Although visual inspection provides a subjective assessment of improvement, it is fundamentally constrained and fails to deliver an accurate or thorough analysis of the algorithm's performance. Therefore, the study used four primary metrics to assess algorithm performance:

1) *The Mean Squared Error (MSE)*: quantifies the average squared deviations between the pixel intensities of the original and enhanced images, functioning as a direct metric for error assessment. If the enhanced and original images match, the MSE should be zero:

$$MSE = \frac{1}{MN} \sum_{i=1}^M \sum_{j=1}^N [I_1(i, j) - I_2(i, j)]^2 \quad (19)$$

where, M and N are the dimensions of the images, $I_1(i, j)$ and $I_2(i, j)$ are the pixel intensities of the original and processed images.

2) *Peak Signal-to-Noise Ratio (PSNR)*: However, when using MSE, an outlier also affects the value, and is highly dependent on the image intensity scale. Therefore, the Peak Signal-to-Noise Ratio (PSNR), the ratio between the maximum power of the original image and the enhanced image in decibels (logarithmic scale), is used to address this deficiency. The enhanced images is better when PSNR is larger:

$$PSNR = 10 \cdot \log_{10} \left(\frac{L^2}{MSE} \right) \quad (20)$$

where, L is the maximum pixel intensity value (e.g. 255 for 8-bit images), MSE is the Mean Squared Error.

3) *Similarity Index Measure (SSIM)*: assesses the similarity of original and enhanced image by analyzing brightness, contrast, and structure, providing a perceptually significant evaluation. Its value should be large for better results:

$$SSIM(x, y) = \frac{(2\mu_x\mu_y + C_1)(2\sigma_{xy} + C_2)}{(\mu_x^2 + \mu_y^2 + C_1)(\sigma_x^2 + \sigma_y^2 + C_2)} \quad (21)$$

where, μ_x and μ_y are the mean intensities of images x and y , σ_x^2 and σ_y^2 are the variances of x and y , σ_{xy} is the covariance between x and y , C_1 and C_2 are small constants to stabilize the division.

4) *Structure Content (SC)*: is the ratio of the sum of squares of the original image pixels to the sum of squares of the enhanced image pixels. The best value of SC is equal to 1 but higher value specifies poor the quality:

$$SC = \sum_{k=1}^K \log \left(\frac{\max(I_k) + \epsilon}{\min(I_k) + \epsilon} \right) \quad (22)$$

where, K is the number of image blocks, I_k is the intensity of the k -th block, ϵ is a small constant to avoid division by zero.

IV. PROPOSED METHOD

The proposed method is divided into two main stages: image quality enhancement and tumor segmentation for Brain MRI.

1) *Image quality enhancement*: This stage consists of two steps: 1) Denoising: The input MRI images are denoised using wavelet shrinkage in the wavelet domain based on Wavelet Packet Transform (WPT), which decomposes the image into higher-resolution frequency components. Thresholding is applied to the detailed components (high-frequency bands that typically contain noise) to suppress noise, followed by an inverse transformation to return the image to the spatial domain. 2) Fine Noise Reduction and Contrast Enhancement: This step includes two parallel processes: a second-stage noise suppression using the Linear Minimum Mean Square Error (LMMSE) filter, and contrast enhancement via morphological transforms. The outputs of these processes are then fused using wavelet fusion to combine the strengths of each approach (see Fig. 2).

2) *Tumor segmentation*: The enhanced images are segmented using the Fast C-means algorithm. The number of clusters is set to the number of main peaks in the intensity histogram. The tumor is assumed to belong to the cluster with the maximum centroid value. Tumor regions are identified through thresholding and refined using morphological post-processing operations (see Fig. 3).

The following subsections detail each step of the proposed method.

A. Image Enhancement

Image enhancement is performed according to the diagram in Fig. 2.

1) *Coarse noise reduction*: In this study, we introduce a multi-stage approach aimed at diminishing different types of noise – particularly Gaussian noise - in MRI images, as demonstrated in Fig. 2. The process begins by applying the Wavelet Packet Transform (WPT) to the noisy image, decomposing it into multiple subbands. Noise reduction is performed using shrinkage threshold on the leaf details components except for the first component. Subsequently, the denoised image is reconstructed using inverse WPT. In this paper, the symlet2 function at level 2 is used, as these are nearly symmetrical wavelets, a modification of the Daubechie function, making them suitable for noise reduction.

2) *Fine noise reduction and contrast enhancement*: Subsequent two concurrent processing methods are employed: Morphological contrast enhancement is used to increase contrast and highlight obscured details. In this paper, a disc-shaped structuring element with a radius of 5 is utilized. The LMMSE filter mitigates Rician noise through the estimation of pixel values derived from local statistical characteristics, effectively minimizing variance while preserving data integrity. This article uses code: LMMSE filter for Rician MRI data written by Santiago Aja-Fernandez (2025). [12]

The results from these two processes are subsequently fused through Wavelet Fusion, which integrates the advantages of noise reduction and contrast enhancement to create image enhancement suitable for subsequent analysis steps.



Fig. 2. Noise reduction flow chart.

B. Tumor Detection

Image enhancement is used for brain tumor detection using Fast C-Means Clustering with the number of clusters selected from the main peaks on the smoothed histogram using the empirical mode decomposition, and the cluster containing the tumor is chosen to correspond to the maximum value of the centroid. Morphological operations such as hole filling, opening, and closing are used to smooth the detected tumor, and regions are used to identify certain characteristics of the tumor. Fig. 3 shows the steps in the segmentation and tumor detection stage. This article uses Fast fuzzy C-means clustering code by Tao-Lei [10]



Fig. 3. Tumor detection flow chart.

C. Dataset and Equipments

This study utilizes the BraTS (Brain Tumor Segmentation) dataset [13], [14], [15], a widely used benchmark for MRI-based brain tumor analysis. The dataset includes multimodal MRI scans (NIFTI (.nii.gz) files), consisting of T1, T1 with contrast enhancement (T1c), T2, and FLAIR sequences. These images are annotated by specialists to delineate key brain tumor subregions: enhancing tumor (ET), tumor core (TC), and peritumoral edema (ED). These segmentations serve as ground truth for evaluating automated segmentation methods. The dataset has been extensively used in research on brain tumor segmentation and classification [16], [17], [18].

The Matlab and Python environment was used for the calculations, and a laptop with Intel Core i.9 CPU, 36GB RAM, and Windows 11 was used for all experiments.

V. EXPERIMENTAL RESULT

This section delineates the outcomes of image enhancement, encompassing denoising and contrast enhancement as well as image segmentation. MRI scan from the BraTS dataset was corrupted to Rician, Gaussian and Salt and Pepper noises at levels of 6%, 8%, 10%, 12%, and 14% to perform image enhancement. The image enhancement process remains uniform across various noise levels; therefore, only results for images at a designated noise level (12%) are visually depicted in the figures, while quantitative assessments for all noise levels are compiled in tables utilizing standard metrics.

A. Image Enhancement

1) Quality analysis:

a) *Image enhancement for rician noise:* Fig. 4 illustrates the denoising outcomes for an MRI scan from the BraTS dataset with 12% Rician noise, utilizing the suggested approach and comparison with Denoising Convolutional Neural Network (DnCNN) and Non-Local Means (NLM). Fig. 4a depicts the original MRI image, which acts as a reference, highlighting distinct structural characteristics crucial for assessing the efficacy of different denoising methods. Fig. 4b illustrates the noisy image, whereby Rician noise considerably obscures tiny details, especially in low-contrast areas, complicating structural interpretation. The outcome of the suggested approach is illustrated in Fig. 4c, showcasing an optimal equilibrium between noise reduction and structural integrity. The image exhibits a little smoother appearance than the original while preserving essential structural elements and texture with minimum distortion. The intensity gradients, especially at the interfaces between brain regions, remain well delineated without the introduction of artifacts. Fig. 4d illustrates the outcome of the NLM approach, which successfully diminishes noise but encounters difficulties in restoring intricate features. Although high-intensity areas are comparatively well-preserved, the pronounced smoothing effect results in the loss of mid-range structural details, causing significant blurriness in essential brain regions. Fig. 4e, illustrates the results of the DnCNN approach, which demonstrates enhanced noise reduction relative to NLM, resulting in a more pristine appearance. This approach, however, creates modest aberrations that manifest as unnatural patterns in regions with abrupt intensity shifts, thus undermining the clinical applicability of the augmented image.

b) *Image enhancement for Gaussian noise:* In addition to Rician noise, we also evaluate the denoising performance under Gaussian noise with 12% corruption. Fig. 5 presents the denoising results for MRI images affected by Gaussian noise using different methods. Fig. 5a the original image serves as a reference. Fig. 5b shows the noisy image that exhibits substantial structural degradation. Fig. 5c shows the outcome of the proposed method, which effectively balances noise removal and structural preservation. Fig. 5d shows the result of NLM method, which reduces noise but blurs fine details. Fig. 5e shows the result of DnCNN, which provides better noise suppression but introduces subtle artifacts; some blurriness remains.

c) *Image enhancement for salt and pepper noise:* Fig. 6 presents the results of image quality enhancement for an image contaminated with 12% Salt and Pepper noise. Fig. 6a shows the original image, while Fig. 6b displays the noise-contaminated image. Fig. 6c shows the image enhancement using our proposed approach, which preserves the brain's intricacies in close proximity to the original image. Fig. 6d shows the results of the NLM method, which effectively smooths the image but obscures certain small details. Fig. 6e displays the results of the DnCNN method, which retains some graininess.

These results demonstrate that our proposed approach maintains essential elements in the image. These visual observations align with the quantitative performance metrics discussed in the next section.

2) *Quantitative analysis:* To assess the denoising effectiveness of the proposed method and other methods across diverse

noise types with different densities from 4, 6, 8, 10, 12 and 14%; the performance quality metrics such as MSE, PSNR, SSIM, and SC are used.

a) *Rician noise:* Table I presents the quantitative metric values for image enhancement calculated from images contaminated with Rician noise at five different noise densities. Except for the SC value, the proposed method demonstrates superior values in MSE, PSNR, and SSIM compared to the other two methods. With low noise density, $\sigma = 6\%$, the MSE of the proposed approach was 88.01, in contrast to DnCNN (279.53) and NLM (287.72). The PSNR of the proposed approach attained 28.69 dB, significantly above DnCNN (23.67 dB) and NLM (23.54 dB). The small MSE value and large PSNR value of the proposed approach exhibited remarkable noise reduction capabilities and greater efficacy in image quality restoration. The proposed method attained an SSIM of 0.43, significantly surpassing DnCNN (0.28) and NLM (0.26). The high SSIM value indicates that the perceived image enhancement of the proposed approach is better than the results of the other two methods. With an SC value of 1.19 for the proposed approach and 0.92 for both DnCNN and NLM, the enhanced image from the proposed approach is slightly inferior in information architecture compared to the other two methods; however, the difference is not substantial and does not affect subsequent analyses. For the remaining threshold levels of 8, 10, 12, and 14% (from cell 2 to cell 5, Table I), the quality assessment results are consistent with the results at the 6% threshold level. Therefore, the quality assessment values in Table I demonstrate that the noise reduction and contrast enhancement capabilities of the proposed method yield better results than the DnCNN and NLM methods when applied to images with Rician noise; consequently, the proposed method is suitable for enhancing the quality of MR images.

b) *Gaussian noise:* Table II presents the quantitative metric values for image enhancement calculated from images contaminated with Gaussian noise at five different noise densities. Except for the SSIM value, the DnCNN method demonstrates superior values in MSE, PSNR, and SC metrics, with the NLM method ranking second and the proposed method ranking third; however, the values of these indices do not differ significantly between the methods. Notably, the SSIM value of the proposed method is the highest and considerably different from the other two methods. From these results, with Gaussian noise, the noise reduction and structural integrity capabilities of the DnCNN method are the highest but not significantly different from the proposed method. Regarding perceptual image quality, the results of the proposed method are the best, as demonstrated by the highest SSIM values across different noise levels and through the visualization shown in Fig. 5.

c) *Salt and Pepper noise:* Table III presents the quantitative metric values for image enhancement calculated from images contaminated with salt and pepper noise at five different noise densities. The MSE and PSNR values show that the noise reduction capability of the DnCNN method is best for the 6% noise level. In contrast, from 8-14% noise levels, the NLM method performs best, with the proposed method ranking second for all threshold levels examined. Regarding the perceptual quality of image enhancement through SSIM values, the NLM method is best at 6-9% noise levels, while

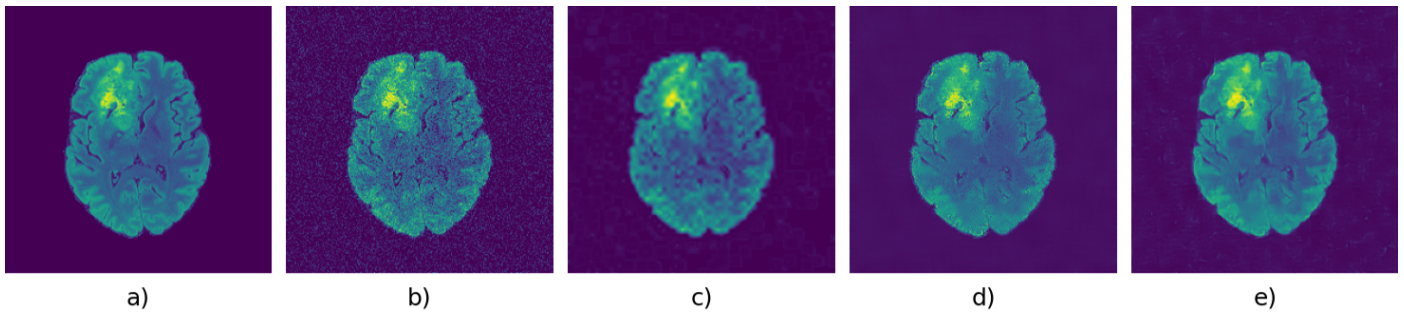


Fig. 4. Enhancement image of 12% Rician noise. a): Original image, b): Noisy image, c): Image enhancement of the proposed approach, d): Image enhancement with NLM method, and e): Image enhancement with DnCNN method.

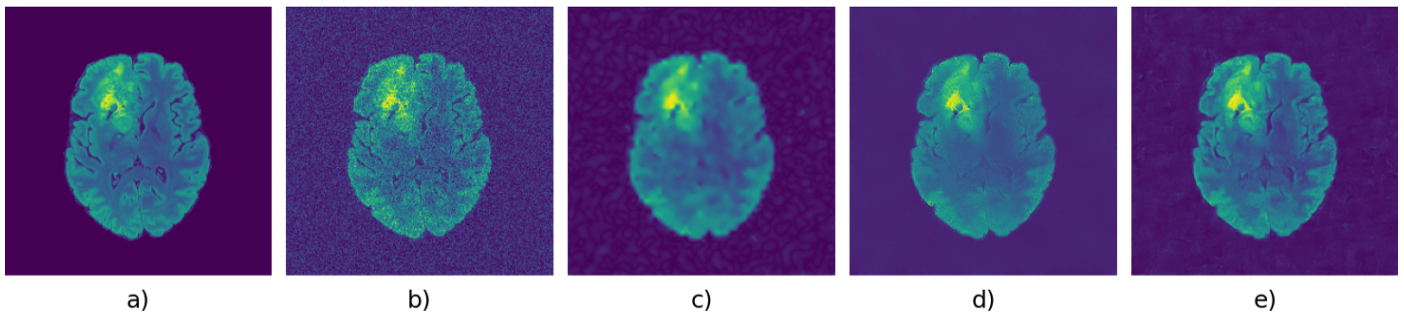


Fig. 5. Enhancement image of 12% Gaussian noise. a): Original image, b): Noisy image, c): Image enhancement of the proposed approach, d): Image enhancement with NLM method, and e): Image enhancement with DnCNN method.

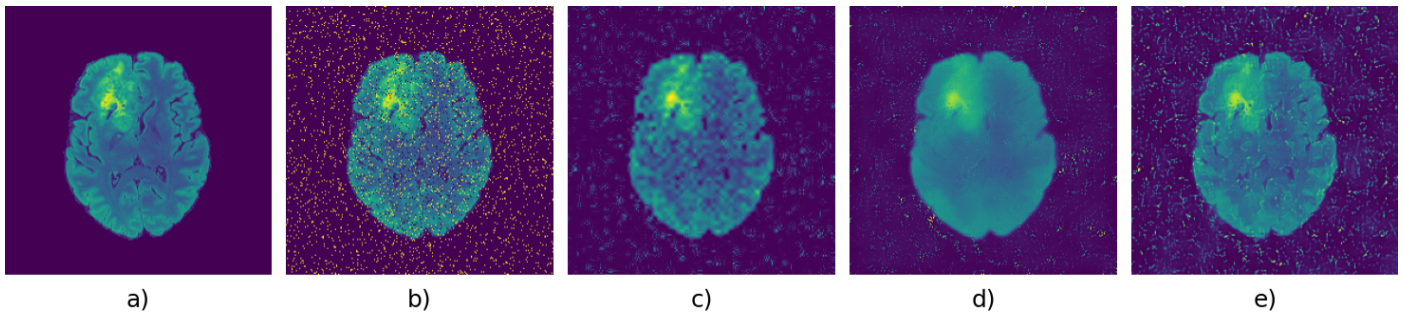


Fig. 6. Enhancement image of 12% Salt & Pepper noise. a): Original image, b): Noisy image, c): Image enhancement of the proposed approach, d): Image enhancement with NLM method, and e): Image enhancement with DnCNN method.

at 10-14% noise levels, the proposed method is superior. For information preservation capability, as indicated by SC values, the proposed approach is best at 6-8% noise levels, and the NLM method is best at 10-14% noise levels.

The positive outcomes in performance indexes suggest that the proposed approach is effective in noise reduction and preserves crucial structural details of brain MR images, making it suitable for the initial processing stage of a CAde system.

3) *Kernel Density Estimate (KDE) analysis:* KDE is probability density estimate smoothed by kernel function. In order to further investigate the image enhancement performance, the KDE of MR images before and after enhancement is analyzed. Fig. 7 shows the KDE of the original image, the image contaminated with Rician noise $\sigma = 12\%$, and the enhanced images. Fig. 7a shows the pixel intensity distribution of the original image exhibits a first mode with a sharp peak and a second mode, which reflects the inherent structure of the brain

MRI including background and tumor. The Rician noisy image shown in Fig. 7b has a broadened intensity distribution, which is characterized by a flattened peak and an extended tail that does not reveal the mode containing the tumor. This distortion indicates a significant loss of structural information caused by the addition of noise, which complicates the extraction of sensible features from the image. The KDE plot of the proposed approach, which is displayed in Fig. 7e, is very similar to the original intensity distribution, demonstrating that image enhancement of the proposed approach restores the original image almost intact, showing high performance of the method. In the KDE from DnCNN in Fig. 7c and NLM in Fig. 7d, distinct differences in their performance are observed. Both recover the mode representing the tumor, but they stretch the first mode causing the background to blur, resulting in lower contrast between the background and the tumor.

In conclusion, the KDE plots indicate that the proposed

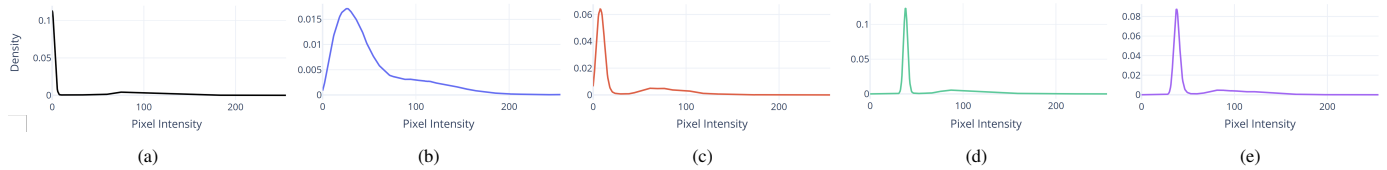


Fig. 7. KDE plot for one MRI image in the dataset. a): Original image, b): Noisy image, c): Image enhancement of the proposed approach, d): Image enhancement with NLM method, and e): Image enhancement with DnCNN method.

TABLE I. QUANTITATIVE METRICS FOR DIFFERENT METHODS WITH RICIAN NOISE AT DIFFERENT NOISE LEVELS

Quantitative metrics				
$\sigma = 6\%$				
Methods	MSE	PSNR	SSIM	SC
Noisy	396.16	22.15	0.20	0.89
DnCNN	279.53	23.67	0.28	0.92
NLM	287.72	23.54	0.26	0.92
Proposed Method	88.01	28.69	0.43	1.19
$\sigma = 8\%$				
Methods	MSE	PSNR	SSIM	SC
Noisy	703.41	19.66	0.16	0.82
DnCNN	490.20	21.23	0.26	0.87
NLM	498.18	21.16	0.24	0.87
Proposed Method	125.34	27.15	0.34	1.24
$\sigma = 10\%$				
Methods	MSE	PSNR	SSIM	SC
Noisy	1097.01	17.73	0.13	0.74
DnCNN	757.90	19.33	0.24	0.80
NLM	767.29	19.28	0.22	0.81
Proposed Method	167.97	25.88	0.29	1.30
$\sigma = 12\%$				
Methods	MSE	PSNR	SSIM	SC
Noisy	1576.86	16.15	0.11	0.66
DnCNN	1085.96	17.77	0.23	0.74
NLM	1096.50	17.73	0.20	0.75
Proposed Method	214.69	24.81	0.25	1.35
$\sigma = 14\%$				
Methods	MSE	PSNR	SSIM	SC
Noisy	2142.38	14.82	0.09	0.59
DnCNN	1474.42	16.44	0.21	0.67
NLM	1486.76	16.41	0.19	0.69
Proposed Method	266.00	23.88	0.23	1.39

TABLE II. QUANTITATIVE METRICS FOR DIFFERENT METHODS WITH GAUSSIAN NOISE AT DIFFERENT NOISE LEVELS

Quantitative metrics				
$\sigma = 6\%$				
Methods	MSE	PSNR	SSIM	SC
Noisy	151.75	26.32	0.26	0.96
DnCNN	47.75	31.34	0.37	1.00
NLM	62.83	30.15	0.36	0.99
Proposed Method	86.02	28.78	0.55	1.18
$\sigma = 8\%$				
Methods	MSE	PSNR	SSIM	SC
Noisy	268.89	23.84	0.20	0.93
DnCNN	76.31	29.30	0.32	0.99
NLM	94.97	28.35	0.30	0.98
Proposed Method	110.25	27.71	0.53	1.24
$\sigma = 10\%$				
Methods	MSE	PSNR	SSIM	SC
Noisy	417.99	21.92	0.16	0.90
DnCNN	109.96	27.72	0.29	0.99
NLM	130.02	26.99	0.26	0.98
Proposed Method	138.51	26.72	0.51	1.30
$\sigma = 12\%$				
Methods	MSE	PSNR	SSIM	SC
Noisy	598.99	20.36	0.13	0.86
DnCNN	149.88	26.37	0.27	0.98
NLM	169.65	25.84	0.24	0.98
Proposed Method	170.58	25.81	0.50	1.37
$\sigma = 14\%$				
Methods	MSE	PSNR	SSIM	SC
Noisy	809.69	19.05	0.11	0.82
DnCNN	195.81	25.21	0.25	0.97
NLM	213.33	24.84	0.22	0.98
Proposed Method	206.88	24.97	0.49	1.45

approach effectively balances noise reduction and structural integrity preservation, as reflected in its intensity distribution closely matching that of the original image. Therefore, image enhancement is well-suited for segmentation and feature extraction.

4) *Segmentation*: Segmentation results for a sample MRI slice from the BraTS dataset are presented in Fig. 8. The figure displays the original image alongside the ground truth tumor mask, followed by the segmented tumors obtained from image enhancement under 12% noise levels of Rician, Gaussian, and Salt and Pepper noise. The results indicate that the segmented tumors closely align with the ground truth, particularly for images enhanced under Gaussian noise, followed by Rician noise, and lastly, Salt and Pepper noise. However, this observation is based on visual inspection.

For quantitative evaluation, five metrics: accuracy, dice coefficient, precision, sensitivity, and specificity—were computed

by comparing the ground truth tumor mask with the detected tumor regions from the enhanced images. These enhanced images were derived from noisy versions of the original MRI slices at varying noise levels, and the results are summarized in Table IV. Since MR images contain tumors that occupy a much smaller area compared to the background, the true negative (TN) value is significantly higher than other evaluation measures. As a result, accuracy and specificity values are close to 1, making them less informative for performance assessment. Therefore, the "precision–sensitivity" pair and the Dice coefficient are used as primary evaluation metrics.

The values in Table IV demonstrate stable tumor segmentation performance across different noise levels. The dice coefficient exhibits a modest rise with elevated noise levels, varying from 0.774 to 0.780 for Gaussian noise and from 0.768 to 0.777 for Rician noise. The dice coefficient diminishes for Salt and Pepper noise from 0.775 to 0.705 with increasing

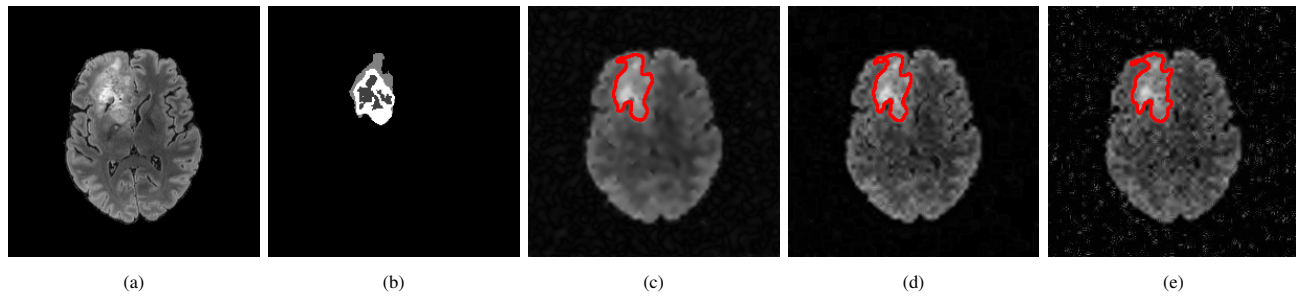


Fig. 8. Segmentation results after denoising for a BraTS 2021 MRI slice. a) Original image, b) Ground truth tumor mask, c) Segmented tumor after denoising 12% Rician noise, d) Segmented tumor after denoising 12% Gaussian noise, e) Segmented tumor after denoising 12% salt-and-pepper noise.

TABLE III. QUANTITATIVE METRICS FOR DIFFERENT METHODS WITH SALT AND PEPPER NOISE AT DIFFERENT NOISE LEVELS

Quantitative metrics				
$\sigma = 6\%$				
Methods	MSE	PSNR	SSIM	SC
Noisy	1703.67	15.82	0.25	0.68
DnCNN	680.59	19.80	0.28	0.85
NLM	771.79	19.26	0.38	0.84
Proposed Method	684.41	19.78	0.23	0.96
$\sigma = 8\%$				
Methods	MSE	PSNR	SSIM	SC
Noisy	2273.34	14.56	0.18	0.61
DnCNN	737.38	19.45	0.24	0.84
NLM	618.40	20.22	0.31	0.89
Proposed Method	685.96	19.77	0.21	1.02
$\sigma = 10\%$				
Methods	MSE	PSNR	SSIM	SC
Noisy	2838.37	13.60	0.13	0.56
DnCNN	778.26	19.22	0.21	0.83
NLM	479.99	21.32	0.25	0.92
Proposed Method	573.57	20.54	0.21	1.16
$\sigma = 12\%$				
Methods	MSE	PSNR	SSIM	SC
Noisy	3405.04	12.81	0.10	0.51
DnCNN	811.97	19.04	0.20	0.83
NLM	403.58	22.07	0.21	0.95
Proposed Method	431.69	21.78	0.27	1.42
$\sigma = 14\%$				
Methods	MSE	PSNR	SSIM	SC
Noisy	3980.13	12.13	0.08	0.48
DnCNN	852.41	18.82	0.19	0.82
NLM	392.01	22.20	0.19	0.96
Proposed Method	471.26	21.40	0.31	1.64

noise levels. Notwithstanding these fluctuations, the values are generally above 70%, signifying a robust concordance between the identified tumors and the ground truth across all noise categories. Optimal tumor segmentation outcomes are attained for images influenced by Gaussian noise, succeeded by Rician noise, and subsequently, Salt and Pepper noise, as indicated by the elevated precision values, which consistently exceed 90%. Sensitivity values, on the other hand, are highest for salt-and-pepper noise, followed by Gaussian noise, and lowest for Rician noise. Nevertheless, sensitivity remains stable within the range of 75–81%, suggesting that the differences in tumor detectability are minimal.

In Table V, the tumor properties of Fig. 8b, c, d and e.

TABLE IV. SEGMENTATION PERFORMANCE METRICS ACROSS NOISE TYPES AND LEVELS

Noise Type	Level	Accuracy	Specificity	Precision	Sensitivity	Dice
Gaussian	6	0.987	0.999	0.976	0.783	0.780
	8	0.987	0.999	0.975	0.783	0.774
	10	0.987	0.999	0.974	0.785	0.775
	12	0.987	0.999	0.971	0.785	0.780
Rician	6	0.986	0.999	0.972	0.780	0.768
	8	0.986	0.999	0.969	0.783	0.771
	10	0.986	0.999	0.964	0.794	0.776
	12	0.986	0.999	0.963	0.794	0.777
Salt-Pepper	6	0.986	0.999	0.963	0.804	0.775
	8	0.985	0.999	0.950	0.809	0.750
	10	0.984	0.999	0.938	0.794	0.750
	12	0.984	0.999	0.946	0.762	0.729
	14	0.984	0.999	0.950	0.750	0.705

Compared to the ground truth (X: 100.52, Y: 82.04, Radius: 24.64), the tumor’s location and morphology are accurately maintained. Under Gaussian noise, there is minor under-segmentation (X: 99.16, Y: 76.81, Radius: 21.94), although the tumor remains discernible. Rician noise exhibits optimal alignment (X: 99.36, Y: 76.77, Radius: 22.12) with negligible variation. Conversely, Salt-Pepper noise induces uneven borders (X: 99.81, Y: 77.63, Radius: 22.97), although the tumor structure remains intact. These results underscore the efficacy of the segmentation method in maintaining tumor shape despite distortions caused by noise.

TABLE V. REGION PROPERTIES ACROSS NOISE TYPES AND LEVELS

Noise Type - Level	X	Y	Radius	Perimeter	Area
Ground Truth	100.52	82.04	24.64	204.37	1908.0
Gaussian	99.16	76.81	21.94	229.86	1512.0
Rician	99.36	76.77	22.12	213.10	1537.0
Salt-Pepper	99.81	77.63	22.97	243.97	1657.0

VI. DISCUSSION

This study introduces a novel enhancement pipeline for brain MRI images that addresses both noise reduction and contrast limitations. Selected for its ability to capture detailed information across all frequency bands and provide better resolution than conventional DWT or SWT techniques, the wavelet packet decomposition (WPD) transform—paired

with the Symlet (“sym2”) wavelet—helps preserve important anatomical structures while reducing Gaussian noise via shrinkage-based denoising.

However, this approach is not without its limitations. First, while shrinkage at WPD level two is effective against Gaussian noise, it is less robust against non-Gaussian artifacts, particularly Rician noise, which is common in MRI. We address this through LMMSE filtering, but the effectiveness of this parallel processing may degrade under very high noise levels or motion artifacts. Second, our contrast enhancement avoids histogram-based distortion by employing morphological operations, yet this technique may underperform in images with extremely low dynamic range or in scans from lower-resolution equipment.

For segmentation, we apply the Tao-Lei variant of the Fast C-means algorithm [10], enhanced by EMD-based adaptive clustering. While this approach improves cluster selection and localization, it depends heavily on the quality of the empirical mode decomposition. Inconsistent IMF extraction, especially in noisy or poorly-contrasted images, can affect the reliability of cluster count estimation and consequently segmentation accuracy.

Another limitation lies in the need for manual parameter tuning for wavelet levels, LMMSE window sizes, and morphological structuring elements. This may reduce scalability across datasets unless an adaptive or learning-based optimization strategy is employed.

Performance validation using visual inspection, quality measures, and KDE plots indicates enhancements compared to baseline approaches like DnCNN and NLM. Nevertheless, our approach currently focuses on 2D axial slices. Extending the framework to handle 3D volumes or dynamic MRI sequences remains a direction for future work.

Notwithstanding these limitations, the synergy of our enhancement and segmentation pipeline provides a promising, integrated preprocessing solution for MRI-based diagnostics. Subsequent research will investigate automated parameter optimization, comprehensive integration with learning-based post-processors, and applicability to various MRI modalities and diseases.

VII. CONCLUSION

In this study, we proposed a new approach for enhancing and segmenting brain MRI images, aiming to improve noise reduction and tumor detection in a clinical context. By combining wavelet packet transform (WPT) denoising, LMMSE filtering, and morphological contrast enhancement—followed by a wavelet-based fusion step—we were able to produce clearer images that retain important anatomical details.

For segmentation, we applied a variant of the C-means clustering algorithm. To improve automation and reliability, the number of clusters was determined using a smoothed histogram, and the tumor region was identified based on the highest intensity centroid. This helped streamline the process of tumor extraction and showed good alignment with ground truth in both visual and quantitative evaluations.

Despite these promising results, some challenges remain. The enhancement and segmentation processes are currently

separate, which may limit their synergy. In future work, we plan to develop a more integrated framework by refining the fusion of enhancement and segmentation steps within our current model-driven approach. Additionally, we will explore automated parameter tuning to improve robustness and scalability. Finally, we intend to validate the method across diverse MRI datasets, including different scanner types and pathological conditions, to ensure broader applicability and clinical relevance.

ACKNOWLEDGMENT

This research is funded by Vietnam National University, Ho Chi Minh City (VNU-HCM) under grant number C2025-18-11.

REFERENCES

- [1] J. M. V. Kinani, A. R. Silva, D. Mújica-Vargas, F. G. Funes, and E. R. Díaz, “Rician denoising based on correlated local features lmmse approach,” *Journal of Medical Systems*, vol. 45, pp. 1–12, 2021.
- [2] M. Hýtch and P. W. Hawkes, *Morphological image operators*. Academic Press, 2020, vol. 216.
- [3] M. Nawaz, R. Qureshi, M. A. Teevno, and A. R. Shahid, “Object detection and segmentation by composition of fast fuzzy c-mean clustering based maps,” *Journal of Ambient Intelligence and Humanized Computing*, vol. 14, no. 6, pp. 7173–7188, 2023.
- [4] C. S. D S and J. Christopher Clement, “Enhancing brain tumor segmentation in MRI images using the IC-net algorithm framework,” *Scientific Reports*, vol. 14, no. 1, p. 15660, Jul. 2024. [Online]. Available: <https://www.nature.com/articles/s41598-024-66314-4>
- [5] I. Dey and S. Siddiqui, “Wavelet transform for signal processing in internet-of-things (iot),” in *Wavelet Theory*. IntechOpen, 2021, p. 183.
- [6] R. Paul, S. Malik, S. Rawat, D. Sharma, M. Alimudeen, A. Professor, and Student, “Edge-preserving image denoising using wavelet packets,” *Journal of Emerging Technologies and Innovative Research*, pp. 570–580, 12 2018.
- [7] S. M. Kay, *Fundamentals of statistical signal processing: estimation theory*. Prentice-Hall, Inc., 1993.
- [8] J. Kubicek, A. Krestanova, M. Polachova, D. Oczka, M. Penhaker, M. Cerny, M. Augustynek, and O. Krejcar, “Design and analysis of lmmse filter for mr image data,” in *Intelligent Information and Database Systems: 11th Asian Conference, ACIIDS 2019, Yogyakarta, Indonesia, April 8–11, 2019, Proceedings, Part II 11*. Springer, 2019, pp. 336–348.
- [9] T. Rahman and M. S. Islam, “Image segmentation based on fuzzy c means clustering algorithm and morphological reconstruction,” in *2021 International Conference on Information and Communication Technology for Sustainable Development (ICICT4SD)*. IEEE, 2021, pp. 259–263.
- [10] T. Lei, X. Jia, Y. Zhang, L. He, H. Meng, and A. K. Nandi, “Significantly fast and robust fuzzy c-means clustering algorithm based on morphological reconstruction and membership filtering,” *IEEE Transactions on Fuzzy Systems*, vol. 26, no. 5, pp. 3027–3041, 2018, code available at: <https://www.mathworks.com/matlabcentral/fileexchange/66181-image-segmentation-using-fast-fuzzy-c-means-clustering>. [Online]. Available: <https://www.mathworks.com/matlabcentral/fileexchange/66181-image-segmentation-using-fast-fuzzy-c-means-clustering>
- [11] J. Anitha, J. D. Peter, and S. I. A. Pandian, “A dual stage adaptive thresholding (dusat) for automatic mass detection in mammograms,” *Computer methods and programs in biomedicine*, vol. 138, pp. 93–104, 2017.
- [12] S. Aja-Fernández, “Lmmse filter for rician mri data,” MATLAB Central File Exchange, 2025, retrieved March 20, 2025. [Online]. Available: <https://www.mathworks.com/matlabcentral/fileexchange/36741-lmmse-filter-for-rician-mri-data>

- [13] U. Baid, S. Ghodasara, S. Mohan, M. Bilello, E. Calabrese, E. Colak, K. Farahani, J. Kalpathy-Cramer, F. C. Kitamura, S. Pati *et al.*, "The rsna-asnr-miccai brats 2021 benchmark on brain tumor segmentation and radiogenomic classification," *arXiv preprint arXiv:2107.02314*, 2021.
- [14] B. H. Menze, A. Jakab, S. Bauer, J. Kalpathy-Cramer, K. Farahani, J. Kirby, Y. Burren, N. Porz, J. Slotboom, R. Wiest *et al.*, "The multimodal brain tumor image segmentation benchmark (brats)," *IEEE transactions on medical imaging*, vol. 34, no. 10, pp. 1993–2024, 2014.
- [15] S. Bakas, H. Akbari, A. Sotiras, M. Bilello, M. Rozycki, J. S. Kirby, J. B. Freymann, K. Farahani, and C. Davatzikos, "Advancing the cancer genome atlas glioma mri collections with expert segmentation labels and radiomic features," *Scientific data*, vol. 4, no. 1, pp. 1–13, 2017.
- [16] P. J. Sørensen, V. A. Liboriussen, F. L. Andersen *et al.*, "Repurposing the public brats dataset for postoperative brain tumor segmentation: Challenges and opportunities," *Tomography*, vol. 10, no. 9, p. 105, 2023.
- [17] J. Petersen, P. Christoph, A.-K. Paul *et al.*, "Multi-class glioma segmentation on real-world data with missing modalities: The smir dataset," *Scientific Reports*, vol. 13, no. 1, p. 15246, 2023.
- [18] A. not specified, "Recent deep learning-based brain tumor segmentation models: A review," *Journal of Imaging Informatics in Medicine*, vol. 2024, pp. 1–19, 2024. [Online]. Available: <https://www.ncbi.nlm.nih.gov/pmc/articles/PMC11298476/>